PHYSICAL REVIEW D **93,** 043019 (2016)

Hydrodynamical study on the conversion of hadronic matter to quark matter. II. Diffusion-induced conversion

Shun Furusawa*

Center for Computational Astrophysics, National Astronomical Observatory of Japan, Osawa, Mitaka, Tokyo 181-8588, Japan

Takahiro Sanada

Department of Science and Engineering, Waseda University, 3-4-1 Okubo, Shinjuku, Tokyo 169-8555, Japan

Shoichi Yamada

Advanced Research Institute for Science and Engineering, Waseda University, 3-4-1 Okubo, Shinjuku, Tokyo 169-8555, Japan

(Received 24 November 2015; published 29 February 2016)

We study transitions of hadronic matter (HM) to three-flavor quark matter (3QM), regarding the conversion processes as combustion and describing them hydrodynamically. Under the assumption that HM is metastable with their free energies being larger than those of 3QM but smaller than those of two-flavor quark matter, we consider in this paper the conversion induced by diffusions of the seed 3QM. This is a sequel to our previous paper, in which the shock-induced conversion was studied in the same framework. We not only pay attention to the jump condition on both sides of the conversion front, but the structures inside the front are also considered by taking into account what happens during the conversion processes on the time scale of weak interactions. We employ for HM Shen's equation of state (EOS), which is based on the relativistic mean field theory, and the bag model-based EOS for quark matter just as in the previous paper. We demonstrated in that paper that in this combination of EOSs, the combustion will occur for a wide range of the bag constant and strong coupling constant in the so-called endothermic regime, in which the Hugoniot curve for combustion runs below the initial state. Elucidating the essential features of the diffusion-induced conversion both in the exothermic and endothermic regimes first by a toy model, we then analyze more realistic models. We find that weak deflagration nearly always occurs and that weak detonation is possible only when the diffusion constant is (unrealistically) large and the critical strange fraction is small. The velocities of the conversion front are $\sim 10^3$–10^7 cm/s depending on the initial temperature and density as well as the parameters in the quark matter EOS and become particularly small when the final state is in the mixed phase. Finally we study linear stability of the laminar weak-deflagration front and find that it is unstable in the exothermic regime (Darrius-Landau instability) but stable in the endothermic regime, which is quite contrary to the ordinary combustions.

DOI: 10.1103/PhysRevD.93.043019

I. INTRODUCTION

The hadronic equation of state (EOS) at supranuclear densities ($\gtrsim 2.8 \times 10^{14}$ g/cm^3), which are believed to prevail at the central region of neutron stars, is still highly uncertain. It is possible that quark matter (QM) exists over a substantial part of a neutron star (such a star is referred to as a hybrid star), and, indeed, the entire star may consist of deconfined quarks [1,2] if three-flavor quark matter (3QM), which is referred to as strange quark matter (SQM) in this case, is the most stable state at zero pressure. SQM is a bulk QM, which is composed of up, down and strange quarks (plus a small fraction of electrons for charge neutrality). If SQM is formed in a neutron star by some mechanism (see, e.g., Refs. [2,3]), which is referred to as a seed in the following, hadronic matter (HM) will be subsequently converted to SQM at the boundary of HM and SQM, and the entire star will be eventually composed of SQM and is called the strange star.

If SQM is the true ground state of strong interactions, HM should be a metastable state, and its decay is avoided by the fact that intermediate states with smaller fractions of strangeness are unstable compared with HM. The conversion of the metastable state to the truly stable state separated by unstable states can be regarded as combustion: HM is a fuel, and SQM is an ash; there is a conversion front in between, in which the mixtures of fuel and ash exist and the conversion process takes place. This conversion region is very thin compared with macroscopic scales, e.g., stellar radii. In the hydrodynamical description of terrestrial

*furusawa@cfca.jp

combustions [4–6], the fuel and ash are related with each other by the so-called Hugoniot relation, and there are in general four combustion modes, strong/weak detonation/deflagration, of which the strong deflagration is thought to be unrealizable. Which mode actually occurs is determined by the conversion mechanism and parameters involved.

Many researchers have investigated with different approaches the combustion modes that are actually realized, the propagation speed of the conversion front [3,7–16] and the global conversion of compact stars [17,18]. There is no consensus yet on how the combustion proceeds in neutron stars [19]. In this pair of papers [20], we study locally the transitions of HM to 3QM from the hydrodynamical point of view. We assume that HM is metastable and has free energies that are higher (or less stable) than those of 3QM but are lower (or more stable) than those of 2QM. Note that it is not necessarily assumed that 3QM is absolutely stable, i.e., the most stable at zero pressure, although the SQM hypothesis is included as a subset. In fact, the SQM hypothesis is not necessary for the conversion from HM to QM [21]. We are just considering the formation of hybrid stars then, and 3QM will be reconverted to HM if decompressed. The SQM hypothesis is necessary, on the other hand, for the existence/formation of strange stars, which would never be converted back to hadronic stars once formed. The main difference from the previous studies is that not only the Hugoniot relation between HM on one side of the conversion front and 3QM on the other side but the structures inside the front are also considered by taking into account what will happen during the conversion processes as well as equations of state (EOSs) in the mixed phase. The length scale of our interest is the one determined by weak interactions, which is actually the width of the conversion front and much larger than the mean free path for strong interactions, whereas it is much smaller than the macroscopic scales, e.g., stellar radii. This justifies the employment of the hydrodynamical description in plane symmetry. We are mainly interested in which combustion modes (strong/weak detonation/deflagration) are likely to be realized for the following two scenarios: (1) the transition via 2QM triggered by a rapid increase in density owing to the passage of a shock wave and (2) the conversion induced by diffusions of a seed 3QM. The former was already reported in the prequel paper [20], and we focus on the latter case in this paper.

We also stress in this pair of papers that for the combination of realistic baryonic EOSs such as the one we employ in this paper and the bag model EOSs for QM, combustions occur for a wide range of a bag constant and/or strong coupling constant in the so-called endothermic regime, in which the Hugoniot curve for combustion runs below the one for the shock wave [20]. Such a combustion has no terrestrial counterpart [4,6] and has been discarded in the previous papers exactly because it is endothermic [12,14,16,17]. We emphasize, however, that there is no reason in fact to throw it away. As long as there is no obstacle in between the initial and final states such as an intermediate state with a higher free energy, reactions proceed spontaneously to realize the free-energy minimum [19,20]. This was confirmed in the shock-induced conversion [20]. In the diffusion-induced conversion we consider in this paper, diffusions of strangeness give rise to the situation where the free energy of the intermediate 3QM is lowered so that it should no longer be an obstacle for conversion. Note also that the terminology of "exothermic/endothermic combustion" is somewhat misleading, since it does not necessarily correspond to heat production/absorption.

In our previous paper, we found that strong detonation always occurs for the transition via 2QM triggered by a rapid density rise in a shock wave. Depending on the values of parameters included in the EOS of QM as well as on the initial density and Mach number of the detonation front in HM, deconfinement from HM to 2QM is either completed or not completed in the shock wave. In the latter case, which is more likely if the EOS of QM ensures that deconfinement occurs above the nuclear saturation density and that the maximum mass of cold quark stars is larger than $2M_{\odot}$, the conversion continues further via the mixed state of HM and 3QM on the time scale of weak interactions. In this paper, we focus on the diffusion-induced conversion for the same parameter sets. The scenario is described more in detail in the next section. Note that our analysis in this paper is local, T; i.e., only the region that just covers the conversion front is taken into account. This is in sharp contrast to the global study of the conversion of entire neutron stars by simulations [17,18]. The two methods are complementary to each other in fact. In the former one can consider in detail, albeit phenomenologically, what is happening inside the conversion region, which cannot be resolved by global simulations. On the other hand, possible backreactions from global configurations as well as boundary conditions cannot be taken into account in the local analysis. We try to list all possible structures that satisfy these necessary conditions but make no further attempt to claim which ones are more likely than others to be realized in the actual global conversion. In this sense, the conditions we consider in this paper are just necessary conditions but not sufficient ones in this pair of papers.

The outline of the paper is as follows. To expedite the understanding of the main results, we give in Sec. II the scenario of the diffusion-induced conversion more in detail and present, employing a toy model, some fundamental features of the combustion fronts for this scenario both in the exothermic and endothermic regimes. The basic equations and EOSs used for QM, HM and the mixed phase in the combustion front are given for a more realistic model in Sec. III, and the main results are presented in Sec. IV. We discuss linear stability of the laminar weak-deflagration

front in Sec. V. The paper is concluded with the summary and discussions in Sec. VI.

II. SCENARIOS AND TOY MODEL

A. Scenarios

The situations we have in mind in this paper are that 3QM has the lower free energy per baryon than HM and 2QM is an obstacle for the conversion from the metastable HM to truly stable 3QM (see Fig. 1 in Ref. [20]). SQM hypothesis is not always assumed, and the critical pressure may exist, below which HM is the most stable and the conversion is forbidden.

In the diffusion-induced conversion, which is essentially the same as the one discussed by Olinto [7], the seed 3QM is assumed to have been already planted somehow, and HM is gradually absorbed by 3QM at their interface. Once engulfed, HM is deconfined to up and down quarks in 3QM, thus reducing the fraction of strangeness. 3QM adjacent to the interface is hence not in β-equilibrium in general, and the chemical equilibration ensues via the production of strange quarks by weak interactions such as $u + e^- \to d + \nu_e$ and $u + d \to u + s$. The process generates a spatial gradient of strangeness and induces its diffusion toward the interface, which in turn compensates for the depletion of strangeness caused by the absorption of HM. Since 2QM is unstable compared with HM, a certain fraction of strangeness is required for the conversion. The critical strangeness fraction is given by the condition that QM with the critical fraction has the same free energy per baryon as HM. Since the strangeness fraction at the interface is maintained by its diffusion from the region with higher fractions, the scenario is referred to as the diffusion-induced conversion.

We draw a schematic picture of the conversion region for this scenario in the left panel of Fig. 1. In this picture, HM is put on the left side of the interface, and QM is located on the opposite side. The interface is assumed to be at rest in this frame (the front-rest frame). The shaded region adjacent to HM is the place where the deconfinement of nucleons takes place. It is accomplished on the time scale of strong interactions, t_s, and hence the width of the deconfinement region is $\lambda_s \sim ct_s \lesssim$ fm with c being the light velocity. As mentioned, the fraction of strangeness is fixed to the nonvanishing critical value (f_{sc} in the figure), at which the free energy per baryon is identical on both sides of the interface between HM and the deconfinement region. What happens in this region may not be described hydrodynamically, and we treat it as a discontinuity with a vanishing width. This is indeed justified, since the conversion region is much more extended as we will see shortly. Following the deconfinement, the β-equilibration of QM occurs, and strange quarks become populated more. Since the strangeness fraction in the asymptotic region, the value in β-equilibrium, is larger than the fraction at the

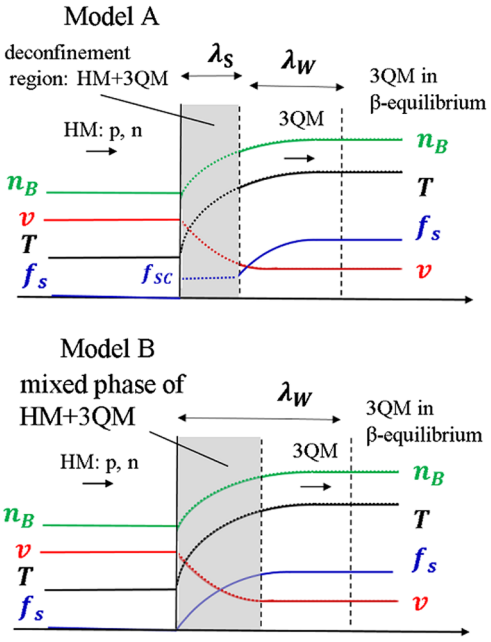

FIG. 1. The schematic pictures of the diffusion-induced conversions considered in this paper. In Model A (left panel), deconfinement may be completed in the time scale of strong interactions to yield a uniform 3QM, which is extended downstream, being β-equilibrated on the time scale of weak interactions. In Model B (right panel), the transition from HM to 3QM proceeds via the mixed phase. As the β-equilibration proceeds, the volume fraction of 3QM increases and reaches unity at some point. Then the β-equilibration goes on in 3QM in the uniform phase. In the figure HM composed of protons and neutrons, which are denoted by p and n, respectively, is put on the left end and 3QM made up of up, down and strange quarks occupies the opposite end. Matter is flowing rightwards in this front-rest frame. The shaded region in the left panel stands for the deconfinement region, the size of which is exaggerated, whereas in the right panel it represents in the right panel the region where the mixed phase exists. The lines labeled as v, n_B, T and f_s show the velocity, baryon number density, temperature and fraction of strange quarks, respectively. Leptons are not shown in this picture. See the text for the meanings of λ_s, λ_w and f_{sc}.

interface, the strangeness diffuses leftward, whereas matter flows rightward in the front-rest frame. Since the β-equilibration is completed on the time scale of weak interactions, t_w, the width of the region, over which it takes place, is given by $\lambda_w \sim v_d t_w$, where v_d is the diffusion velocity, and is evaluated as $\lambda_w \sim 10^{-4}$–10^{-1} cm for the typical values of $v_d \sim 10^4$–10^7 cm/s and $t_w \sim 10^{-8}$ s. We hence obtain the relation $\lambda_s \ll \lambda_w \ll R$ with R being the representative macroscopic scale such as the radius of a neutron star. This justifies our hydrodynamical treatment of this region, which we refer to as the *conversion region* in this paper.

We have so far assumed that the 3QM, which is extended to the right of the interface with HM, is in the uniform phase from right after the transition. This may not be the

case, though. In fact, we find in some cases that the free energy is lowered if one considers the mixed phase. Since we do not take into account the surface energy in this estimation, which tends to hamper the appearance of the mixed phase, this is certainly inconclusive, but we cannot exclude the possibility, either. We hence study it also, referring to it as model B in the following. The right panel of Fig. 1 depicts what we have in mind. As described more in detail in Sec. III D, we introduce the volume fraction of 3QM, which is less than unity unless the uniform 3QM has the lowest free energy. In the mixed phase, the pressure equilibrium is assumed between HM and 3QM. We further impose chemical equilibrium for up and down quarks between HM and 3QM. As strangeness increases via diffusion, so does the volume fraction of 3QM. And at some point (or from the beginning in some cases), the uniform 3QM is obtained. The final state of 3QM is achieved even later through the β-equilibration, which takes place on the time scale of weak interactions, t_w.

Although we are mostly interested in the possible structures in the conversion region, the Hugoniot relations that connect the asymptotic states are no less important. They are obtained from the conservations of baryon number, momentum and energy. Figure 2 shows some of the representative Hugoniot curves for realistic EOSs of HM and 3QM, in which the relativistic formulation is employed. We can see that the Hugoniot curves run below and/or to the left of the initial point in three out of four cases, which implies that the combustions occur in the endothermic regime. An intriguing thing with this regime is the fact that there is no Jouget point and the detonation branch is connected with the deflagration branch without a gap in the initial velocity. It is also interesting to point out that for some parameters, e.g., $B^{1/4} = 140$ MeV and $\alpha_s = 0.6$, the Hugoniot curve is terminated at some point and cannot be extended to lower pressures, since the temperature would become negative. It is found that the Hugoniot curve for combustion runs above the initial state only for rather small bag constants as demonstrated for the model with $B^{1/4} = 125$ MeV. Such combustions are said to be exothermic and are similar to terrestrial combustions. The Hugoniot curves were presented for different combinations of EOS parameters, and their trend was discussed more in detail in Sec. II B of our previous paper [20]. In this paper we discuss, based on the processes and structures in the conversion region, which combustion modes are likely to be realized both in the exothermic and endothermic regimes. In the rest of this paper, we employ a nonrelativistic formulation, which is well justified for the diffusion-induced conversion, since the fluid velocity is typically much smaller than the light velocity.

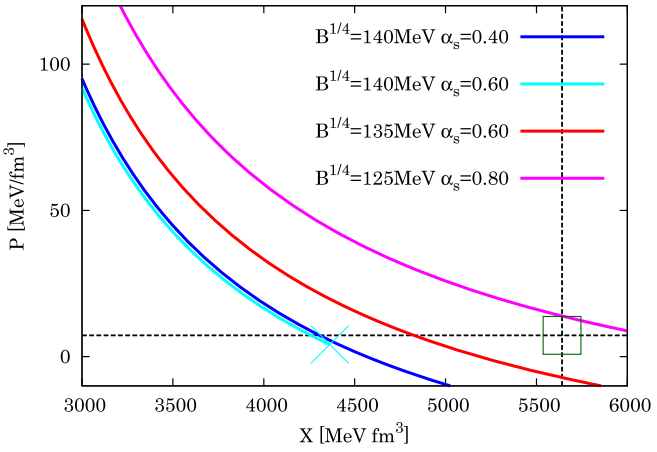

FIG. 2. The Hugoniot curves for various values of the bag and strong coupling constants. $X = (h\rho)/n_B^2$ is the relativistic analog to the specific volume which is indeed reduced to the specific volume in the non-relativistic limit [20,22]. Here h is the specific enthalpy. The initial state of HM is assumed to be PNS matter at $T = 10$ MeV, $Y_p = 0.3$ and $\rho_i = 3.0 \times 10^{14}$ g/cm^3, which is indicated by the square. The cross marks the point, at which zero temperature is obtained.

B. Formulation of toy model

We now turn our attention to the structures in the conversion region that connects the initial and final asymptotic states. We assume the plane symmetry and consider one-dimensional stationary profiles of matter flows that undergo the phase transition from HM to 3QM. The assumption of plane symmetry and stationarity is well justified, since the width of the conversion region is much smaller than the typical macroscopic length scale and the time, during which matter stays in this region, is much shorter than the time scale, on which the initial hadronic state is changed either by the propagation of the conversion front in the (proto-)neutron star or by the adjustment of (proto-)neutron-star configuration to the appearance of the quark phase. In this section, we introduce a toy model that will facilitate our analysis and understanding of the main results presented in Sec. III. The simplification is mainly concerning EOSs. As shown shortly, it is indeed a very crude approximation to reality, but it still captures qualitatively the essence of the more realistic model introduced in the next section. There is also an advantage in the toy model that we can freely change the behavior of Hugoniot curves, particularly the regime of combustion. We hence believe that this simplified model is worth presenting here.

The basic equations to describe the stationary structures of the conversion region are the conservation equations of mass, momentum and energy in the front-rest frame, which are unchanged in the more realistic models introduced in the next section and given by

$$\rho v = \rho_i v_i (= \rho_f v_f), \tag{1}$$

$$P + \rho v^2 = P_i + \rho_i v_i^2 (= P_f + \rho_f v_f^2), \tag{2}$$

$$h+\frac{1}{2}v^2 = h_i+\frac{1}{2}v_i^2\left(=h_f+\frac{1}{2}v_f^2\right), \tag{3}$$

where plane symmetry is assumed; an x coordinate is introduced, and the initial HM is assumed to be located at $x=-\infty$, and the final 3QM is assumed to be realized at $x=+\infty$; ρ, v, P and h are the baryon density, fluid velocity, pressure and specific enthalpy, respectively; and the subscripts i and f stand for the initial and final states. These equations are complemented by another equation that gives the spatial distribution of strangeness,

$$v\frac{df_s}{dx}-D\frac{d^2f_s}{dx^2}=\frac{f_{s,f}-f_s}{\tau}, \tag{4}$$

where f_s is the fraction of strangeness and $f_{s,f}$ is its asymptotic value in the final state; the diffusion coefficient for strangeness is denoted by D, and τ gives the time scale of β-equilibration; they are varied rather arbitrarily in the toy model to see the dependence of solutions on these parameters. Divided by $f_{s,f}$, the above equation is rewritten as

$$v\frac{d\bar{f}_s}{dx}-D\frac{d^2\bar{f}_s}{dx^2}=\frac{1-\bar{f}_s}{\tau} \tag{5}$$

for $\bar{f}_s=f_s/f_{s,f}$.

The strange quarks are populated up to the boundary between HM and QM (see the left panel of Fig. 1). The critical fraction of the strange quark (f_{sc} in Fig. 1) is given by hand arbitrarily in this toy model, whereas it is determined consistently with EOSs in the more realistic model. Since the β-equilibration ensues for the fraction of strange quark greater than this critical value, the time scale τ is set to infinity otherwise.

We employ the so-called γ-law EOS both for HM and QM, knowing that this is certainly an oversimplification,

$$P_{HM}=(\gamma-1)\rho\epsilon, \tag{6}$$

$$P_{QM}=(\gamma-1)\rho(\epsilon+e), \tag{7}$$

where the upper equation is for HM and the lower is for QM; γ, ρ and ϵ are the adiabatic index, baryon density and specific internal energy, respectively. The EOS for QM is different from that for HM in that the former includes an extra term, e, in the specific internal energy, which is utilized to control the regime of combustion; with a positive e, we have an exothermic combustion and vice versa.

In the conversion region, QM has strangeness fractions that are different from the asymptotic values. In this section, we assume for simplicity that these states are also described by the γ-law EOS as

$$P=(\gamma-1)\rho(\epsilon+\bar{f}_s e), \tag{8}$$

where we multiply the extra energy, e, by the fraction of strange quark, $\bar{f}_s$, introduced above, thus interpolating the intermediate 2QM ($\bar{f}_s=0$) and final 3QM ($\bar{f}_s=1$) very crudely. These treatments will be much improved in Sec. III. Since we are interested in the qualitative features of the conversion regions in this section, this level of approximation is sufficient.

We normalize all quantities by adopting an appropriate density, pressure and time, for which we normally take the initial density, pressure and weak interaction time scale. Then the parameters that characterize the system are the normalized diffusion coefficient, $D^*=D/(c_{si}^2\tau)$, and extra energy, $e^*=e/c_{si}^2$, with sound velocity of HM, c_{si}, and τ.

C. Results of toy models

In the following we analyze the solutions to the equations given above [Eqs. (1)–(3) and (5) together with Eqs. (6)–(8)]. The exothermic ($e>0$) and endothermic ($e<0$) cases are discussed in turn separately.

1. Exothermic case ($e>0$)

We first consider the exothermic case with $e>0$, i.e., the ordinary combustion as observed on Earth. The Hugoniot curve for combustion then runs above the initial sate in the $P-V$ diagram.

The typical solutions for the diffusion-induced scenario are displayed in Fig. 3. In these calculations, we take $D^*=1.0$ and $e^*=0.2$. Note that only the QM region ($x\geq 0$) is shown, since all quantities are constant in the HM region ($x<0$). In the left panel, the solution for $\bar{f}_{sc}=0.8$ is presented, whereas the right panel corresponds to $\bar{f}_{sc}=0.1$. We find that the former solution is a weak deflagration and the latter is a weak detonation. This is most evident in Fig. 4, in which this and other solutions are displayed together with the Hugoniot curve in the $P-V$ plane. The initial state corresponds to the point (1,1) in this diagram, owing to the normalization. For $\bar{f}_{sc}=0.8$ as well as $\bar{f}_{sc}=0.6$, the specific volume V increases whereas the pressure decreases as the matter changes to the final state on the Hugoniot curve. This is a feature that characterizes the weak deflagration in the ordinary combustion. For $\bar{f}_{sc}=0.1$ and 0.2, on the other hand, the specific volume and pressure change in the opposite direction, which is evidence for detonation. Note also that in both cases, the final states are closer to the initial states than the Jouget point is, implying that they are weak combustions. It is also found from the figure that the final state approaches the Jouget point on each branch as $\bar{f}_{sc}$ decreases (increases) in the weak deflagration (detonation).

The change of combustion mode with the value of f_{sc} is also demonstrated in Fig. 5, where some integral curves are shown in the $d\bar{f}_s/dx-\bar{f}_s$ diagram, where x is normalized with $v_i\tau$. Note that the system of equations is reduced to a single, second-order, ordinary differential equation for $\bar{f}_s$,

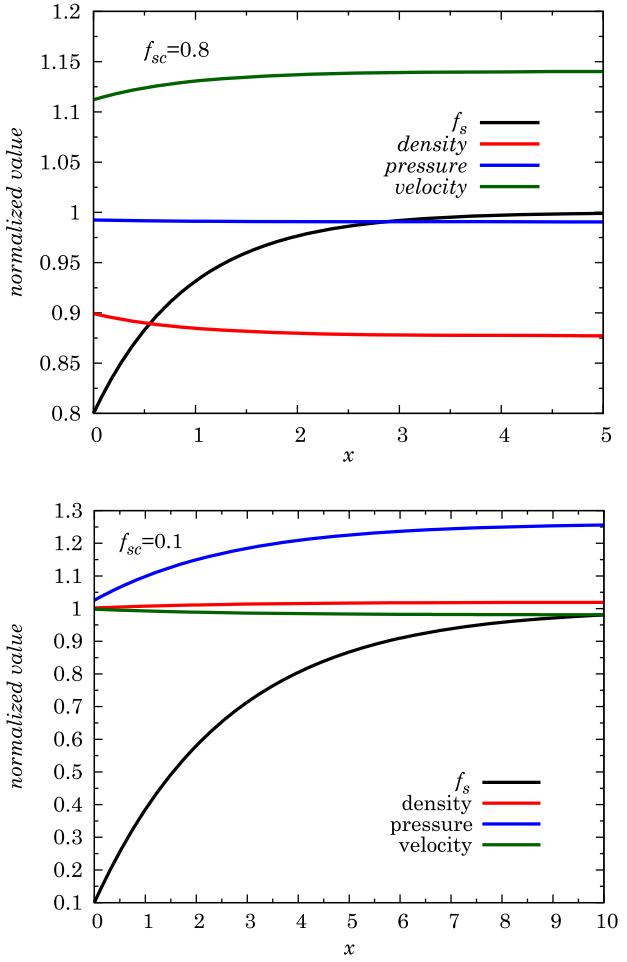

FIG. 3. The evolutions of the strangeness fraction, density, pressure and velocity. The critical fractions of strangeness are $f_{sc} = 0.8$ (left panel) and 0.1 (right panel). The strangeness fraction and the other values are normalized by the values in the final and initial states, respectively.

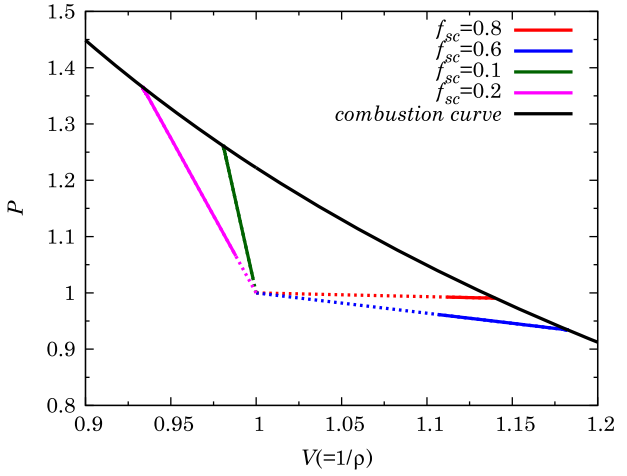

FIG. 4. Solutions for different critical fractions of strangeness in the toy model presented in the P-V diagram. The dotted lines correspond to the deconfinement regions, which may not be described hydrodynamically and treated as discontinuity in this paper.

$$\frac{d^2\bar{f}_s}{dx^2} = \frac{M_i^2}{D^*}\left(\frac{(\gamma M_i^2+1) \pm \sqrt{(M_i^2-1)^2 - 2(\gamma^2-1)M_i^2 e^* \bar{f}_s}}{(\gamma+1)M_i^2} \times \frac{d\bar{f}_s}{dx} + \bar{f}_s - 1\right), \tag{9}$$

where M_i is the Mach number of the flow in HM and the upper/lower signs correspond to weak detonation/deflagration. In the left column of the figure, the integral curves for weak deflagration are shown, whereas those for weak detonation are displayed in the right column. The integral curve we seek is the one that runs into the point with $\bar{f}_s = 1.0$ and $d\bar{f}_s/dx = 0.0$. For $\bar{f}_{sc} = 0.8$ there is a solution only in the weak deflagration regime, which is drawn in red in the figure. As the value of $\bar{f}_{sc}$ decreases, the final state is close to the lower Jouget point, and at a certain point the solution ceases to exit as mentioned above. This is demonstrated in the middle panels, where the integral curves are presented for $\bar{f}_{sc} = 0.4$. In neither regime do we find a solution. As the value of $\bar{f}_{sc}$ decreases further, however, there appears a solution again, and the final state moves to the upper branch. In the bottom panels we show the integral curves for $\bar{f}_{sc} = 0.1$. In this case the solution exists in the weak detonation regime. It is important that the mode change is automatically obtained by solving the structure in the conversion region. It should be also noted that the diffusion-induced conversion is not equivalent to the weak deflagration.

So far the diffusion constant is fixed to be $D^* = 1.0$. As it gets smaller, the region of $\bar{f}_{sc}$ that gives weak detonation becomes narrower; i.e., the Jouget point is reached at smaller values of $\bar{f}_{sc}$. If we take a realistic value of the diffusion constant, $D \sim 1\ \mathrm{cm}^2/\mathrm{s}$ $(D^* \sim 10^{-13})$, no weak detonation is obtained for $\bar{f}_{sc} \gtrsim 10^{-4}$. This suggests that, although in principle the diffusion-induced conversion is not equivalent to weak deflagration, in reality that may be the only solution realized. This will be confirmed in the next section by the more realistic model, in which $\bar{f}_{sc}$ is not a free parameter but is determined consistently with the EOSs employed for HM and QM.

2. Endothermic case ($e < 0$)

Now we proceed to the endothermic case ($e < 0$). The Hugoniot curve for combustion runs below the initial point. Like the exothermic case, there are two states that satisfy the Rankine-Hugoniot jump conditions for a given pair of (V, P) and a velocity v. Unlike the ordinary combustion, however, we always find one of them to the left and the other to the right of the initial state in the $P - V$ diagram. These combustions are classified by the same scheme as for the exothermic case: detonation is a combustion mode, for which the initial state is supersonic in the front-rest frame, whereas deflagration is a combustion with a subsonic initial velocity; if the final state is

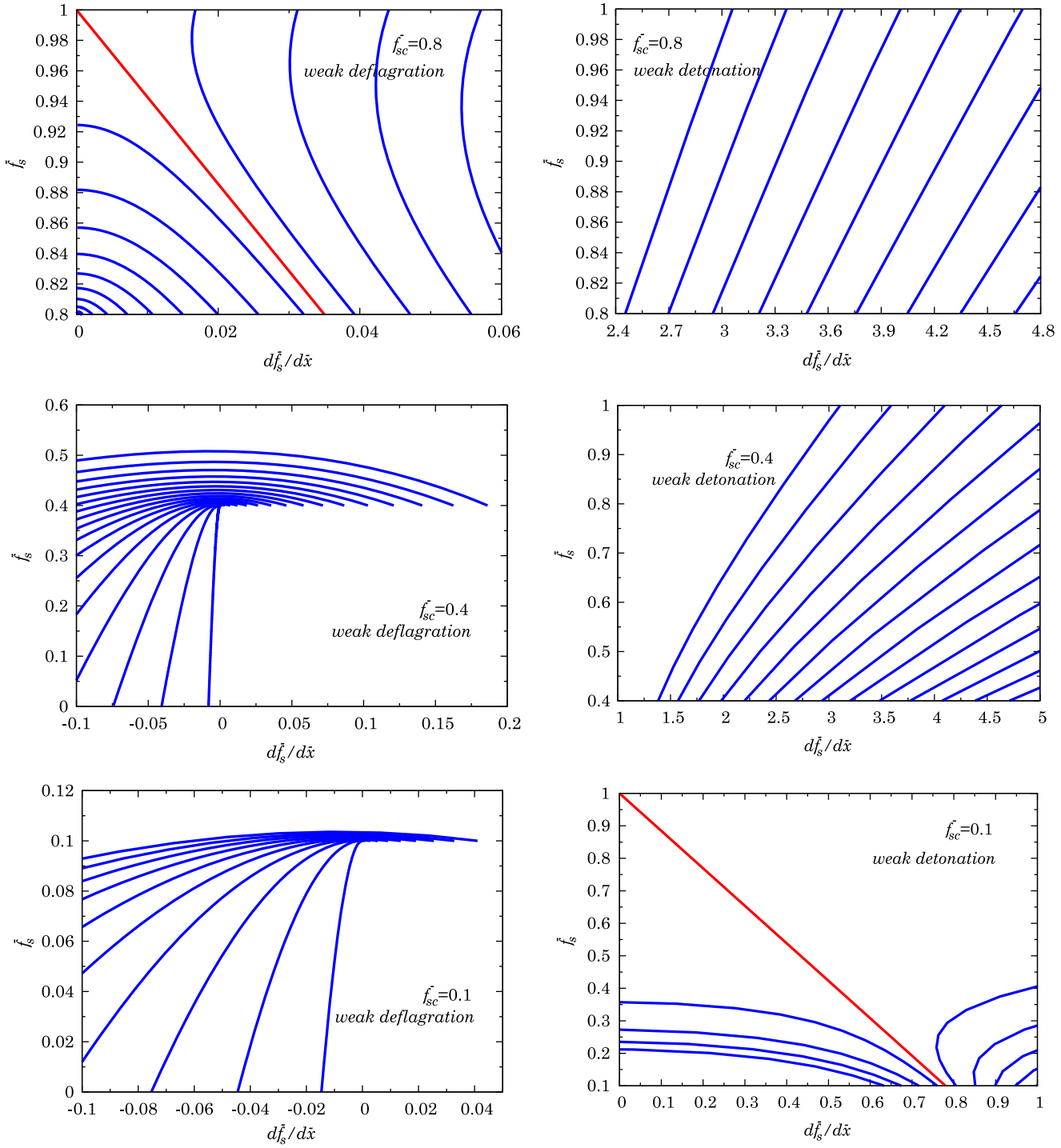

FIG. 5. Integral curves in the $d\bar{f}_s/dx - \bar{f}_s$ diagram for different values of the critical strangeness fraction, $\bar{f}_{sc}$. The left column corresponds to the weak deflagration regime whereas the right one represents the weak detonation regime. The solutions we seek are the integral curves that run into the point with $\bar{f}_s = 1.0$ and $d\bar{f}_s/dx = 0.0$ and are drawn in red in the figure. For large values of $\bar{f}_{sc}$, the solution is found in the weak deflagration regime (top row) whereas weak detonations are obtained for small values of $\bar{f}_{sc}$ (bottom row). Note that there is a parameter range in between, in which there is no solution either in the weak deflagration or in the weak detonation regime, as shown in the middle row.

subsonic, the combustion is either strong detonation or weak deflagration; on the other hand, it is called either weak detonation or strong deflagration if the flow in the final state is supersonic. One interesting feature in the endothermic combustion is that there is no Jouget point and the detonation branch is connected with the deflagration branch without a gap in the initial velocity.

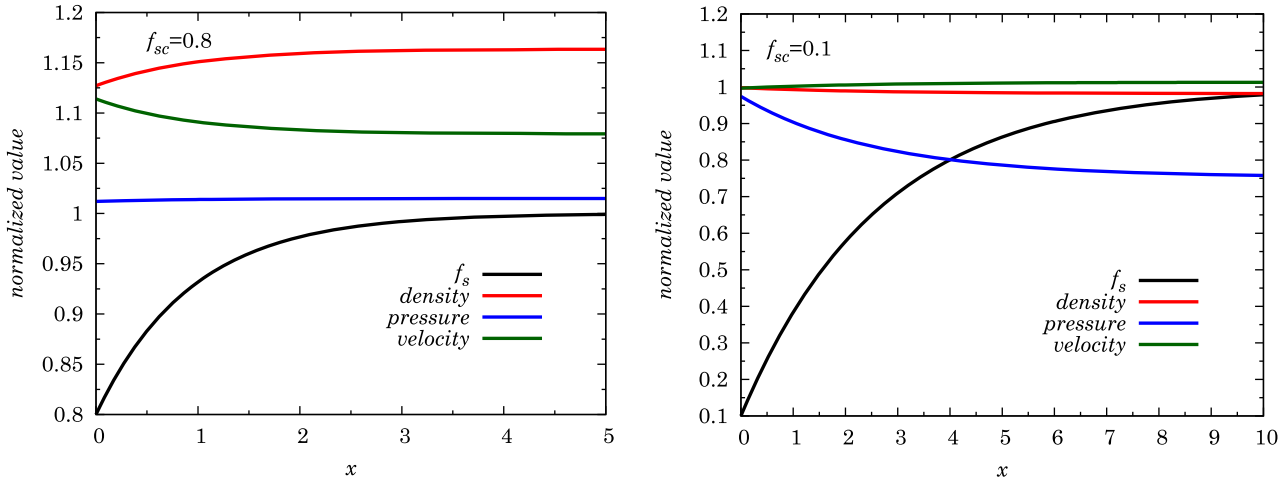

FIG. 6. The evolutions of the strangeness fraction, density, pressure and velocity in the endothermic case. The left and right panels are for $\bar{f}_{sc} = 0.8$ and $\bar{f}_{sc} = 0.1$, respectively. The strangeness fraction and the other values are normalized by the values in the final and initial states, respectively.

It turns out that the solutions are similar to the exothermic counterpart: for $D^* = 1.0$, weak deflagration obtains for relatively large $\bar{f}_{sc}$, whereas weak detonation is realized for small values. They are shown in Fig. 6. In the upper panels, the distributions of various quantities as a function of position are displayed for $\bar{f}_{sc} = 0.8$ in the left panel and for $\bar{f}_{sc} = 0.1$ in the right panel. The corresponding trajectories are given with other cases in the $P - V$ diagram in Fig. 7. The endothermic nature is reflected in the fact that the specific volume decreases (increases) and the pressure increases (decreases) in weak deflagration (weak detonation); i.e., the sense is opposite to the exothermic counterparts. The integral curves in the $d\bar{f}_s/dx - \bar{f}_s$ plane are presented in Fig. 8.

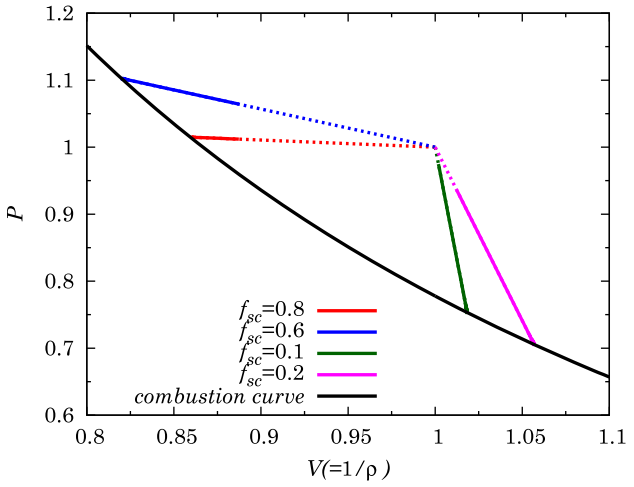

FIG. 7. The trajectories in the P-V diagram for different critical fractions of strangeness in the endothermic case. The dotted lines correspond to the deconfinement regions, which may not be described hydrodynamically and treated as discontinuity in this paper.

Just like in the exothermic case, weak detonation is suppressed as the value of diffusion coefficient D is diminished. As a matter of fact, we do not find weak detonation for the realistic value $D \sim 1.0$. It is hence surmised that, although the diffusion-induced conversion is not equivalent to weak deflagration in principle, in reality it is the only combustion mode realized also in the endothermic case. This will be confirmed by more realistic models in the next section. Note in passing that matter is compressed in weak deflagration in the endothermic case.

III. FORMULATION OF REALISTIC MODEL

A. EOSs for HM and QM

The EOSs we employ for HM and QM are the same as those in the previous paper [20]. Shen's EOS [23] is adopted for HM; it is based on the relativistic mean field theory, in which nuclear interactions are described by exchanges of mesons. This EOS is rather stiff, having the incompressibility of 281 MeV and the symmetry energy of 36.9 MeV, and the maximum mass of cold neutron star is $2.2M_\odot$. We employ the MIT bag model for QM, which takes into account the confinement and asymptotic freedom of quarks phenomenologically and describes QM as a collection of freely moving quarks in the perturbative vacuum with a vacuum energy density given by the so-called bag constant, B. The first-order corrections with respect to the strong coupling constant, α_s, are also taken into account [24,25]. The masses of quarks are set to be $m_{up} = 2.5$, $m_{dn} = 5.0$ and $m_{sg} = 100$ MeV [26], where the subscripts of up, dn and sg stand for up, down and strange quarks, respectively.

In Fig. 9, we summarize the properties of 2QM and 3QM as well as of quark stars for some combinations of the bag and strong coupling constants. The crosses correspond to models investigated in this paper and listed in Table I of the

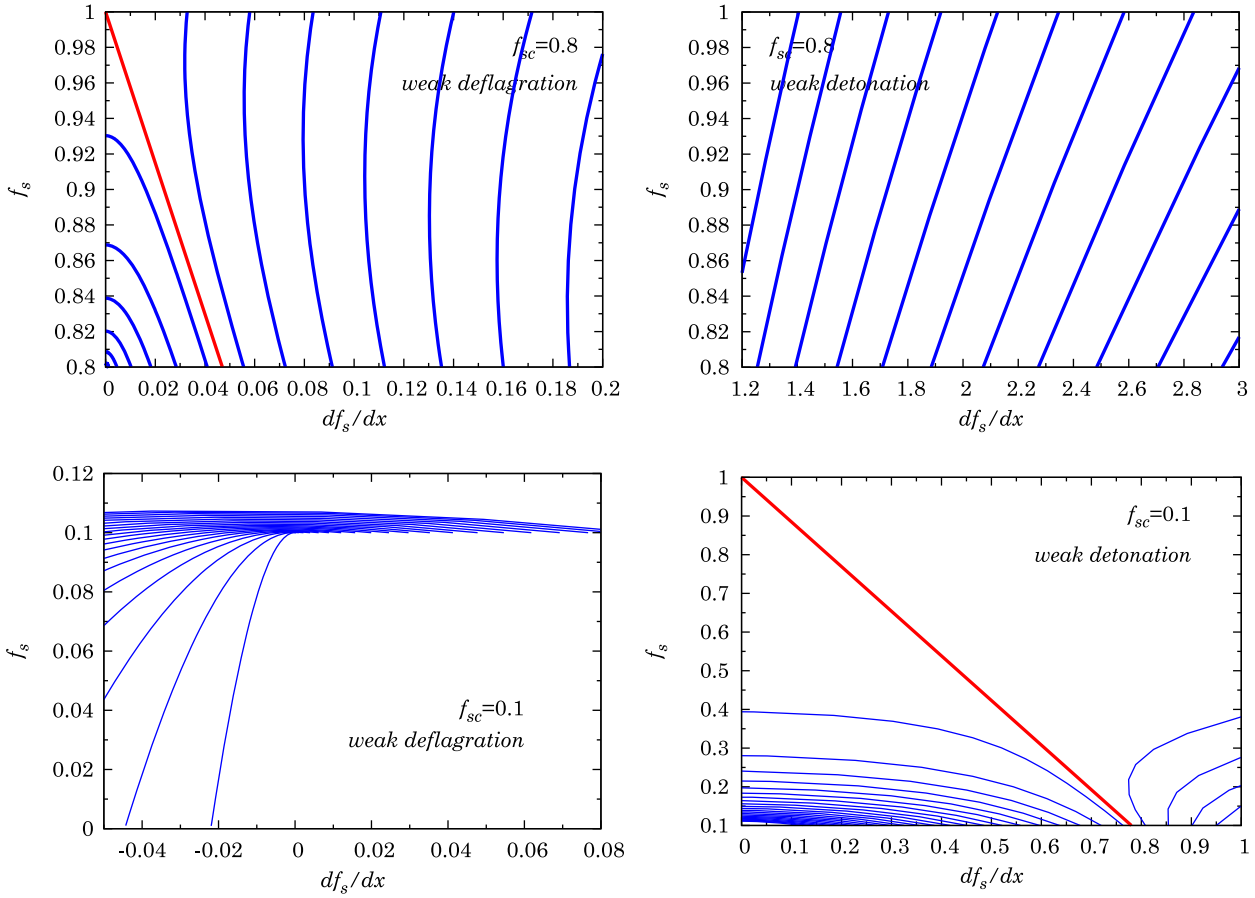

FIG. 8. The phase diagrams for the toy model in the endothermic regime. The left column corresponds to the weak deflagration whereas the right one represents weak detonation. The top panels are for $\bar{f}_{sc} = 0.8$ and the bottom ones are for $\bar{f}_{sc} = 0.1$.

previous paper [20]. They all satisfy the requirement that 2QM in vacuum should have a larger energy per baryon than that of HM (∼934 MeV) including surface effects [27]. For some models, the SQM hypothesis holds with the energies per baryon of 3QM being smaller than ∼930 MeV. Although the critical density, at which HM converts itself to 2QM spontaneously, plays no role in the diffusion conversion, we choose pairs of B and α_s so that the critical density should be larger than the initial density. Furthermore, it is ensured that the maximum mass of cold quark stars is larger than $2M_\odot$.

B. Asymptotic states

In the following subsections, we explain our descriptions of various regions in Fig. 1. We start with the asymptotic regions of the two states, from one of which the conversion begins and with the other of which it ends. The former is called fuel in combustion, and the latter is referred to as ash. We take the x coordinate from the fuel at $x \to -\infty$ to the ash at $x \to \infty$. The fuel of our interest is composed of neutrons and protons as the hadronic component and electrons and neutrinos as the leptonic component. They are assumed to be in charge neutrality and β-equilibrium. In the case of proto-neutron star (PNS) ($T \sim 10$ MeV), neutrinos are assumed to be trapped and equilibrated with matter, whereas they are assumed to be absent in the case of cold neutron star (NS). The lepton fraction Y_{lep} is assumed to be $Y_{lep} = 0.3$ everywhere for the PNS case. The electron fraction in the NS matter is determined from the conditions of β-equilibrium without neutrinos and of charge neutrality. On the other hand, the thermodynamic state of the ash or 3QM in β-equilibrium is derived from the conditions $\mu_{up} + \mu_e = \mu_{dn} + \mu_{\nu_e}$ and $\mu_{sg} = \mu_{dn}$. More details about the asymptotic states are given in Sec. IV B in our previous paper [20].

C. Model A: Jump condition for the transition from HM to pure 3QM

As mentioned earlier, we consider in this paper two possible ways of the transition from HM to QM. In this and next subsections, we will describe them in turn more in detail. In model A, we assume that once matter trespasses the interface of HM and QM, HM is simply deconfined to up and down quarks and mixed into the 3QM that has the critical strange fraction, f_{sc}, on the time scale of strong interactions, t_s. At the interface between the HM and the 3QM, they are hence supposed to have the same free

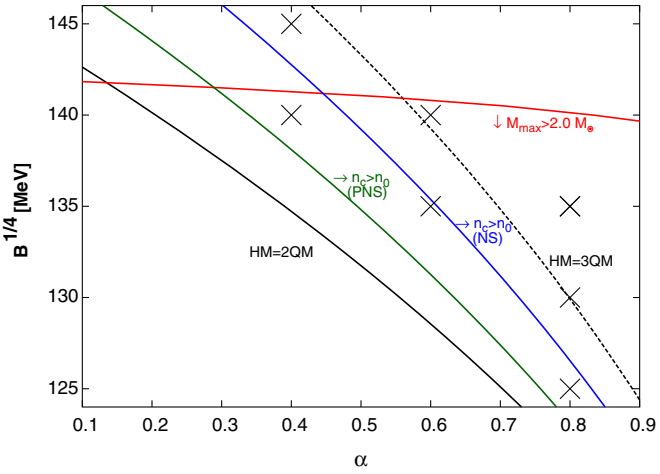

FIG. 9. Some constraints on the values of the bag constant and strong coupling constant. The black solid and dashed lines show the pair, for which the energy per baryon of HM coincides with that of 2QM and with that of 3QM, respectively. The domain to the left of the former line is excluded, since HM would be unstable to the deconfinement to 2QM. The red curve is the critical line, above which the maximum mass of quark star would become smaller than $2M_\odot$, the largest pulsar mass observed so far. The green and blue solid lines indicate the pairs, for which the critical density of the spontaneous transition from HM to 2QM occurs at the nuclear saturation density. See Sec. IV A in the previous paper [20] for more details. The crosses correspond to the models listed in Table I of that paper.

energy. Given the initial state of HM, we can then calculate various quantities in the 3QM just next to the interface as follows,

$$n_{\nu_i} = n_{\nu_Q}, \tag{10}$$

$$n_{e_Q} = \frac{2n_{up} - n_{dn} - n_{sg}}{3}, \tag{11}$$

$$\frac{2n_p + n_n}{n_{B_i}} = \frac{n_{up}}{n_{B_Q}}, \tag{12}$$

$$G_i = G_Q, \tag{13}$$

in addition to the conservative equations [Eqs. (1)–(3)]. The subscripts Q and i indicate the quantities for the 3QM and the initial state of HM, respectively. In the last equation, G_Q and G_i denote their free energies, respectively. Neutrinos essentially do not interact with other particles during this transition, and their number density and temperature do not change [Eq. (10)]. It hence occurs that neutrinos and matter have different temperatures just after the transition. Electrons are swiftly redistributed to ensure charge neutrality [Eq. (11)], since their plasma frequency is very high. Equation (12) means that the fraction of the up quark is conserved. The value of f_{sc} is determined self-consistently by Eq. (13).

D. Model B: Transition via the mixed state of HM and 3QM

In model B, we assume that HM is not mixed into QM uniformly but the phase separation occurs at first. As the strange fraction increases due to the diffusion, the volume fraction of HM is lowered, and a uniform 3QM is realized at some point ($x = x_a$). The β-equilibration continues further until the final state of 3QM in β-equilibrium is reached. In the mixed phase, we assume then that the chemical potentials of protons and neutrons are equal to those in 3QM:

$$\mu_p = 2\mu_{up} + \mu_{dn},$$
$$\mu_n = \mu_{up} + 2\mu_{dn}.$$

Neutrinos and electrons are assumed to be uniform spatially and satisfy

$$\mu^H_{\nu_e} = \mu^Q_{\nu_e},$$
$$\mu^H_e = \mu^Q_e,$$

where the indices H and Q mean the values in the hadron and quark phases, respectively. In this paper we do not consider the surface energy associated with the phase boundary and take into account the bulk volume fraction of QM, which is denoted by r in the following. We then assume in the mixed phase that charge neutrality is ensured only globally: $n_e = (1-r)n_p + r(2n_{up} - n_{dn})/3$. It is also assumed as a common practice that the temperatures and pressures on both sides of the phase boundary are equal to each other:

$$P^H = P^Q, \tag{14}$$

$$T^H = T^Q. \tag{15}$$

Note that the above conditions should be satisfied locally at each position x in the region that the mixed phase occupies. All quantities are hence not constant in space but depend on x. On the other hand, the lepton fraction is assumed to be constant over the entire region. It is emphasized again that the volume fraction of QM is obtained as a result of the minimization of the free energy. If the uniform QM is favored in terms of the free energy, it is realized automatically. In this sense, model B includes model A.

E. Diffusion of strange quarks

The diffusion of strange quarks may be described approximately for the strange quark fraction, $f_s = n_{sg}/(3n_B)$, as follows,

$$u\frac{df_s}{dx} - D\frac{d^2 f_s}{dx^2} = \frac{f_{s_{eq}} - f_s}{\tau}, \tag{16}$$

where τ is the time scale of weak interactions that enforce β-equilibration, $\sim 10^{-8}$ s, and D is the diffusion constant, ~ 1 and $\sim 10^6$ cm^2/s for PNS and NS matter, respectively. The second term on the left-hand side represents the diffusion, whereas the right-hand side describes the β-equilibration in the relaxation approximation. Although the diffusion constant depends in general on the temperature and chemical potentials of quarks [7], we assume that it is constant for simplicity. We also solve the following differential equation for Y_{up},

$$u\frac{dY_{up}}{dx} = \frac{Y_{up}^{eq} - Y_{up}}{\tau}, \tag{17}$$

where Y_{up} is the fraction of the up quark: $Y_{up} = (1-r)Y_{up}^{H} + rY_{up}^{Q}$.[1] The hydrodynamical conservation equations, Eqs. (1)–(3), and the charge neutrality [together with Eqs. (14) and (15) for model B] give the fractions of other particles. The boundary conditions for these differential equations are given in the next subsection.

In model A, we suppose that after deconfinement, the neutrino temperature and lepton fractions in QM ($x > 0$), which are denoted by $T_{\rm lep}$ and $Y_{\rm lep}$, respectively, change gradually toward the equilibrium values on the time scale of weak interactions and assume that they are approximately described as follows:

$$u\frac{dY_{\rm lep}}{dx} = \frac{Y_{\rm lep}^{\rm eq} - Y_{\rm lep}}{\tau}, \tag{18}$$

$$u\frac{dT_{\rm lep}}{dx} = \frac{T_{\rm lep}^{\rm eq} - T_{\rm lep}}{\tau}. \tag{19}$$

In model B $Y_{\rm lep}$ is constant, and we adopt the same diffusion constant both in the mixed phase ($x < x_a$) and in the uniform 3QM ($x > x_a$), since the mean free pass and thermal velocity ($\sim c$) of strangeness are more or less the same. When we solve Eq. (16), f_s is the strange fraction in quark phase alone: $f_{s_Q} = n_{sg}/(n_{up} + n_{dn} + n_{sg})$. Note that the uniform quark phase may not be attained and the mixed phase survives even in the final state for some models with large B and/or α (see Sec. IV in Ref. [20]). It is obvious that model A cannot be applied to such cases. As mentioned earlier, the appearance of the mixed phase will depend sensitively on the surface energy we neglect in this paper.

F. Numerical method

Here we briefly explain how to solve numerically the equations given above. We suppose that the interface of HM and QM is at rest at $x = 0$. We first choose the initial thermodynamic state in HM at $x = -\infty$. Since the HM is uniform at $x < 0$, we only attempt to obtain solutions for QM at $x > 0$. For that purpose, we employ the shooting method for the velocity of HM at $x = -\infty$, which is single unknown quantity in HM. More precisely, we first make a guess on the value of the velocity; then the gradient of the strangeness fraction at $x = 0_+$ is obtained as $df_s/dx|_{x=0_+} = u_i f_s/D$ from the condition that the strangeness should not trespass the interface at $x = 0$; the strangeness fraction itself (f_{sc} for model A and f_{sQ} for model B) is determined by solving the junction condition at the interface (model A) or at the phase boundary (model B); the diffusion equation together with other equations is then solved toward $x = +\infty$; if the initial guess is correct, the solution so obtained approaches smoothly an asymptotic state, i.e., a state in β-equilibrium with $f = f_s^{\rm eq}$ and $df_s/dx = 0$; otherwise we modify the guess and repeat the above steps over. We iterate this procedure until the correct value of the velocity of HM and, as a result, the solution are obtained.

IV. RESULTS OF REALISTIC MODELS

In the following we present the numerical results obtained for the realistic models. Conversions from PNS matter are discussed first, and those from cold NS matter are considered thereafter. We assume that PNS matter has the temperature $T = 10$ MeV and lepton fraction $Y_{\rm lep} = 0.3$ including neutrinos initially. The diffusion constant is estimated as $D \sim 10^{-3}(\mu_{\rm quark}/T)^2$ cm^2/s and chosen to be $D = 0.9$ cm^2/s in most of the cases, corresponding to $\mu_{\rm quark} = 300$ MeV. We notice that we do not stick with the formation of the diffusion constant and take various values. We adopt other values as well, however, and study its influences. The time scale of weak interactions is set to $\tau = 10^{-8}$ s.

We begin with the solutions for $B^{1/4} = 140$ MeV and $\alpha_s = 0.4$ and the initial density of 3.0×10^{14} g/cm^3 both in models A and B. The left panel of Fig. 10 shows the fractions of various particles, which are defined as n_i/n_B with n_i being the number density of particle i. For model A, we find that 3QM has the critical strangeness fraction $f_{sc} = 0.049$ at $x = 0_+$ right after deconfinement. The number of down quarks is the largest of three quarks, since neutrons are more numerous than protons in HM($x < 0$). Strange quarks increase rather quickly at first, and their fraction approaches the asymptotic value more slowly later.

The distributions of thermodynamical quantities are shown in the right panel of Fig. 10. The speed of the conversion front is found to be $\sim 2.3 \times 10^4$ cm/s. It will hence take about a minute to convert a neutron star to a strange star, if the velocity does not change much in the neutron star. The pressure is almost constant, since the velocity is very small and the ram pressure is negligible in momentum conservation [Eq. (2)]. The temperature is dropped at the interface ($x = 0_+$), since the deconfinement to 3QM with low f_s is endothermic in the literal sense. This was also found in the deconfinement from HM to 2QM in our previous paper [20].

[1] $r = 1$ in model A.

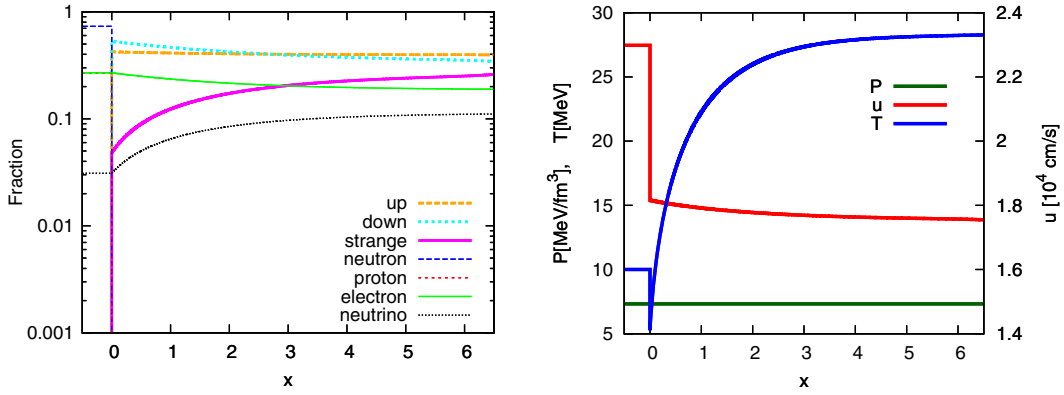

FIG. 10. Fractions of various particles (left) and the pressure, velocity and temperature (right) for Model A with $B^{1/4} = 140$ MeV and $\alpha_s = 0.40$. Each fraction is defined to be the ratio of the number density of the particle to the baryonic number density. The x coordinate is normalized by the typical length of weak interactions, $\sqrt{D\tau}$.

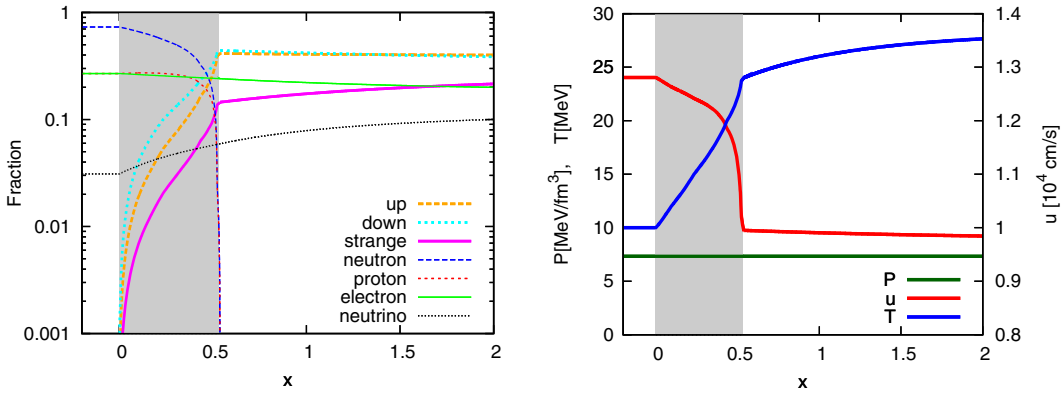

FIG. 11. Fractions of various particles (left) and the pressure, velocity and temperature (right) for Model B with $B^{1/4} = 140$ MeV and $\alpha_s = 0.40$. The shaded region stands for the region in the mixed phase.

Figure 11 displays the solution for model B, in which the mixed phase is taken into account. Again quarks start to populate at $x = 0$, but in this case QM is surrounded by HM in the mixed phase. The volume fraction of QM increases as x becomes larger, and QM occupies the entire volume ($r = 1$) at $x_a = 0.5$. From this point on, the β-equilibration continues in the uniform QM mainly through the conversion of down quarks to strange quarks until the β-equilibrium is reached at $x \sim 2$. The speed of the conversion front is $\sim 1.3 \times 10^4$ cm/s, and the pressure is almost constant just in the same way as in model A. The temperature is not decreased in model B since f_{s_Q} of 3QM in the mixed phase has a large enough value from the beginning to guarantee an exothermic deconfinement.

We compare the trajectories in the $n_B - T$ plane for models A and B in Fig. 12. Models with another combination of EOS parameters $B^{1/4} = 135$ MeV and $\alpha_s = 0.60$ are also shown. The mixed phase ends in model B at points $(n_B, T) = (0.21, 21)$ and $(0.23, 24)$ for the models with $B^{1/4} = 140$ MeV and $\alpha_s = 0.40$ and $B^{1/4} = 135$ MeV and $\alpha_s = 0.60$, respectively. Models A and B merge at these

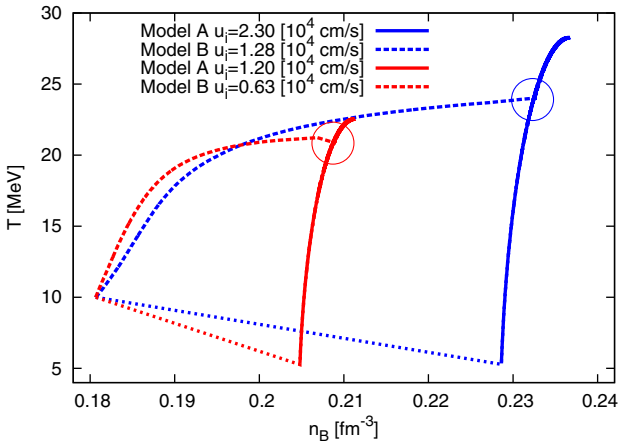

FIG. 12. The trajectories in the $n_B - T$ plane for Models A (solid lines) and B (dashed lines). $B^{1/4}$ and α_s are 140 MeV and 0.40 for red lines and 135 MeV and 0.60 for blue lines. Dotted lines represent jumps at $x = 0$ in Model A. Circles indicate the points where the uniform phase is reached in Model B. The two models coincide with each other thereafter.

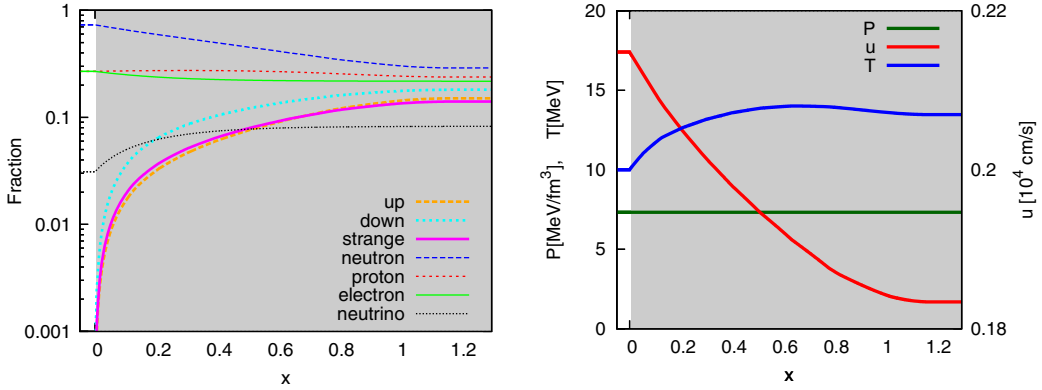

FIG. 13. Fractions of various particles (left) and the pressure, velocity and temperature (right) for Model B with $B^{1/4} = 140$ MeV and $\alpha_s = 0.60$. The shade stands for the region in the mixed phase.

points as marked with circles and have the same values of $f_s = 0.14$ and 0.19. In model A, there appears a 3QM with a rather small value of $f_{sc} = 0.049$ and 0.099 at $x = 0_+$ for the same combinations of EOS parameters. The formation of the mixed phase is favored in terms of the free energy for 3QM with such small f_s as long as the surface energy is ignored.

As shown shortly, no solution is obtained for model A if the final state is in the mixed phase. The results for model B with $B^{1/4} = 140$ MeV and $\alpha_s = 0.60$ are shown in Fig. 13. The mixed phase of HM and 3QM survives up to the final state, in this case, which is in sharp contrast to the previous case with $B^{1/4} = 140$ MeV and $\alpha_s = 0.40$ (Fig. 11). This is because the energy of QM is higher for larger B and/or α_s (see Sec. IV A in Ref. [20]). The front velocity in this case is $\sim 0.2 \times 10^4$ cm/s, somewhat smaller than that in the previous case. Figure 14 compares the results of four models, i.e., those with $B^{1/4} = 135$ MeV and $\alpha_s = 0.6$ and $B^{1/4} = 135$ and $\alpha_s = 0.70$ in addition to those presented already in Figs. 11 and 13. The final state for $B^{1/4} = 135$ MeV and $\alpha_s = 0.70$ is a mixed state of HM and 3QM just as for the model with $B^{1/4} = 140$ MeV and $\alpha_s = 0.60$ shown in Fig. 13, whereas a uniform 3QM results for $B^{1/4} = 135$ MeV and $\alpha_s = 0.60$ as for the model in Fig. 11.

It is found that the final densities are higher for larger B because the EOSs become softer. On the other hand, the final temperatures are lower for larger α_s, since the (absolute value of the negative) latent energy for deconfinement is greater and deconfinement is incomplete with the final states in the mixed phase. These features do not depend on the critical fraction of strangeness as shown in Fig. 15, where we compare different models that have the strangeness fraction at $x = 0_+$ either of $f_{s_Q} = 0.1$ or of $f_{s_Q} = 0.2$. In all cases, the final states are pure 3QM. We can confirm that the final density depends only on $B^{1/4}$ and the final temperature is lower for larger α_s. These trends are also seen in the shock-induced conversion [20]. The front velocity is mainly determined by f_{s_Q} via the boundary

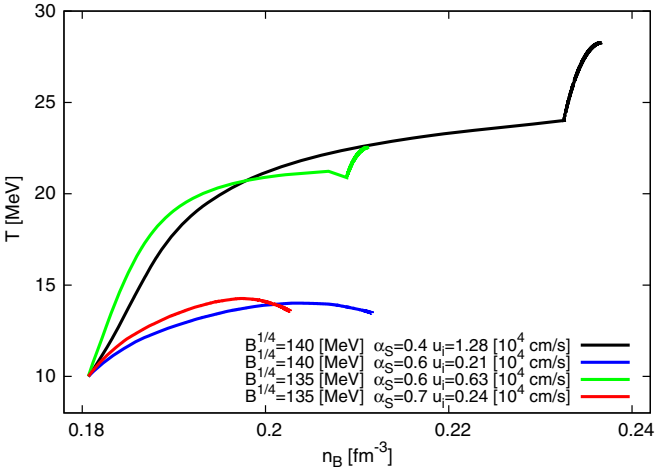

FIG. 14. The trajectories in the $n_B - T$ plane for models with different EOS parameters. $B^{1/4}$ and α_s are 140 MeV and 0.40 (black), 140 MeV and 0.60 (blue), 135 MeV and 0.60 (red), and 135 MeV and 0.70 (blue).

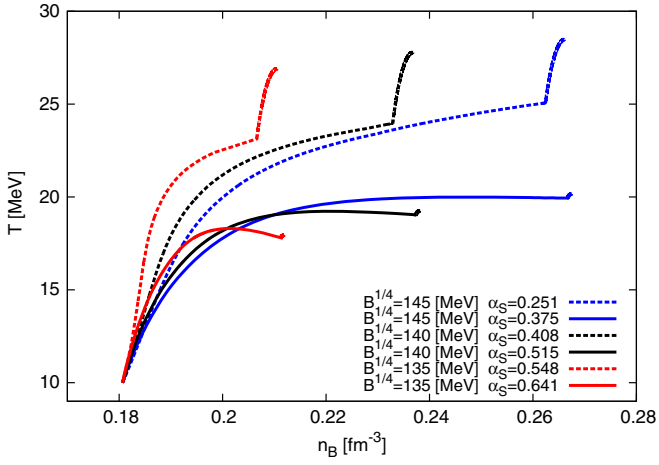

FIG. 15. The trajectories in the $n_B - T$ plane for the models with $B^{1/4} = 135$ MeV (red), 140 MeV (black) and 145 MeV (blue), which have the same strangeness fractions at $x = 0_+$: $f_{s_Q} = 0.10$ (dashed lines) or 0.20 (solid lines).

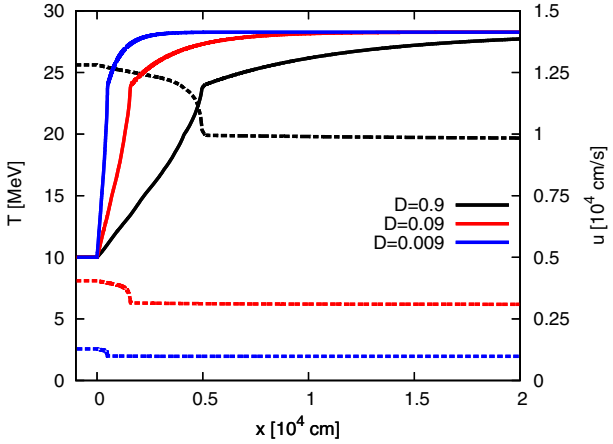

FIG. 16. The velocity (dashed lines) and temperature (solid lines) for different diffusion constants: $D = 0.9$ (black) 0.09 (red) 0.009 (blue) cm^2/s. The EOS parameters are $B^{1/4} = 140$ MeV and $\alpha_s = 0.40$.

condition, although it is a bit larger for larger B, $u_i = 4.11$, 4.28 and 4.48×10^4 cm/s for $B^{1/4} = 135$, 140 and 145, respectively, in the case of $f_{s_Q} = 0.1$, whereas in the case of $f_{s_Q} = 0.2$, $u_i = 11.3, 11.6$ and 12.1×10^4 cm/s for the same bag constants.

In the models presented so far, the diffusion constant is fixed to 0.9 cm^2/s, the value evaluated from $D \sim 10^{-3}(\mu_{\rm quark}/T)^2$ with the initial temperature and chemical potentials of quarks. Figure 16 demonstrates how the results are modified for different values of D in the model with $B^{1/4} = 140$ MeV and $\alpha_s = 0.40$. The qualitative behavior of the temperature and velocity as well as other quantities (not shown in the figure) is similar, although it is different quantitatively. We find that the front velocity and the thickness of mixed phase are both proportional to the square root of the diffusion constant, $\lambda_w \propto \sqrt{D}$ and $u_i \propto \sqrt{D}$, which is similar to that of Alford *et al.* [15].

Although the diffusion coefficient D is assumed to be constant here for simplicity, it will get smaller in reality as the temperature is increased. Then the mixed state will be thinner than that obtained here. Note, however, that the final temperature is twice the initial temperature at most.

The initial density is another important parameter. The front velocity becomes larger, and the mixed state gets wider as the initial density increases as shown in Fig. 17. The model with $\rho_i = 2.5 \times 10^{14}$ g/cm^3 ends up with the final state in the mixed phase, since the energy difference between 3QM and HM is small at low densities. The strangeness fraction at the end of the mixed phase is also affected by the initial density, $f_s = 0.145$ for $\rho_i = 3.0 \times 10^{14}$ g/cm^3, whereas $f_s = 0.127$ for $\rho_i = 3.5 \times 10^{14}$ g/cm^3; i.e., the uniform 3QM is reached even with these small values of f_s if the initial density is high.

We have so far observed that weak deflagration is always obtained in the realistic models with $B^{1/4} \gtrsim 130$ MeV, which are all in the endothermic regime for PNS matter as shown in Fig. 2. This conclusion is also not changed for the exothermic regime. Figure 18 displays the result for the model with $B^{1/4} = 125$ MeV and $\alpha_s = 0.80$ as an example in the exothermic regime. In this model matter expands in the mixed phase and is slightly compressed thereafter ($x \gtrsim 0.62$), although the pressure is almost constant. Note that the final number density should be larger (smaller) than the initial one if weak detonation occurs in the exothermic (endothermic) regime. It is clear from the right panel of Fig. 18 that weak deflagration results in both regimes. This is in agreement with the results obtained with the toy model that weak deflagration is the unique outcome of the diffusion-induced conversion as long as we take a realistic value of the diffusion coefficient.

Finally, we mention the solutions for the NS matter, in which β-equilibrium is assumed to be established initially at $T = 0.01$ MeV. The model parameters are set to be $B^{1/4} = 130$ MeV, $\alpha_s = 0.80$, $\rho_i = 3.0$ or

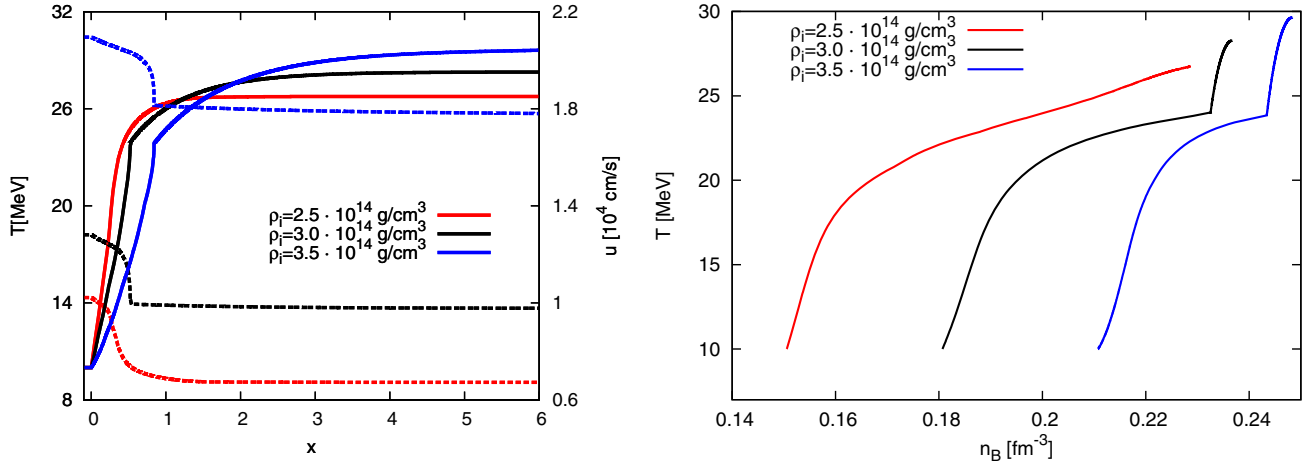

FIG. 17. The velocity (dashed lines) and temperature (solid lines) distributions (left) and the trajectories in the $n_B - T$ plane (right) for the models with $\rho_i = 2.5$ (red), 3.0 (black) and 3.5 (blue) g/cm^3. The EOS parameters are $B^{1/4} = 140$ MeV and $\alpha_s = 0.40$.

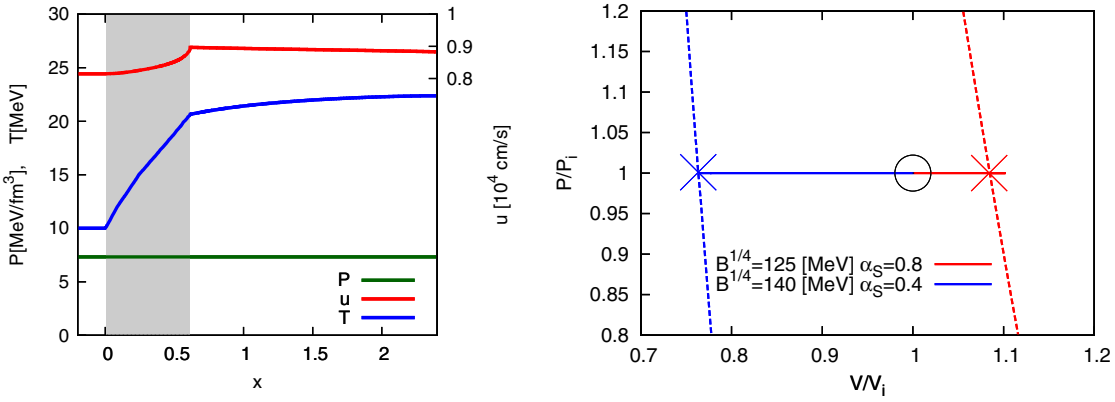

FIG. 18. (left) the pressure, velocity and temperature distributions for the model with $B^{1/4} = 125$ MeV, $\alpha_s = 0.80$ and (right) the trajectories (solid lines) in the $P - V$ plane and the Hugoniot curves for combustion (dashed lines) in the exothermic regime ($B^{1/4} = 125$ MeV, $\alpha_s = 0.80$, red) and in the endothermic one ($B^{1/4} = 140$ MeV, $\alpha_s = 0.40$, blue). The initial and final states are indicated by the circle and crosses, respectively.

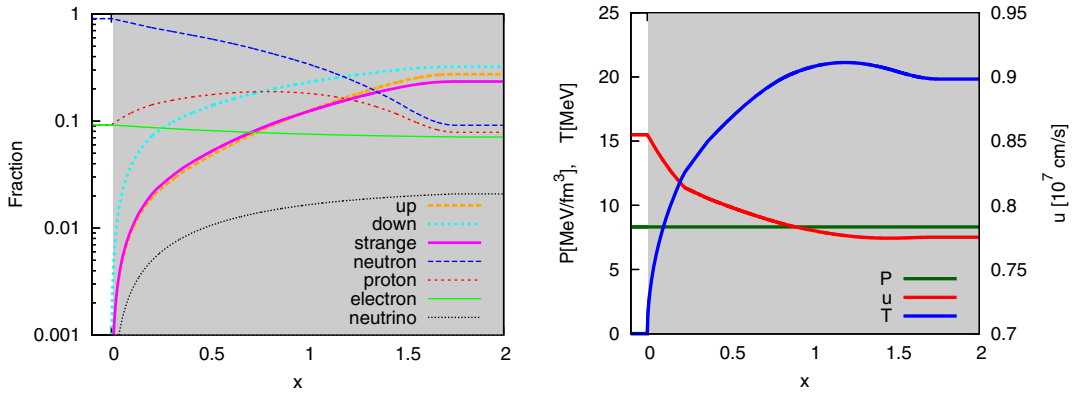

FIG. 19. The same as Fig. 13 but for NS matter with $\rho_i = 3.0 \times 10^{14}$ g/cm^3, $B^{1/4} = 130$ MeV and $\alpha_s = 0.80$.

5.6×10^{14} g/cm^3 and $D = 9.0 \times 10^5$ cm^2/s according to the initial temperature. In these cases, the final states are in the mixed phase as shown in Figs. 19 and 20. Again the width of the conversion region should get narrower in reality as the temperature rises, since the diffusion coefficient would be reduced. The results are not much different from those of the corresponding PNS cases. The velocity of the conversion front is larger, $\sim 10^7$ cm/s, owing to the greater diffusion constant. Neutrinos, which are absent initially, start to populate with strange quarks via weak interactions at $x > 0$. In the case of $\rho_i = 5.6 \times 10^{14}$ g/cm^3, the density is increased at first by the emergence of the

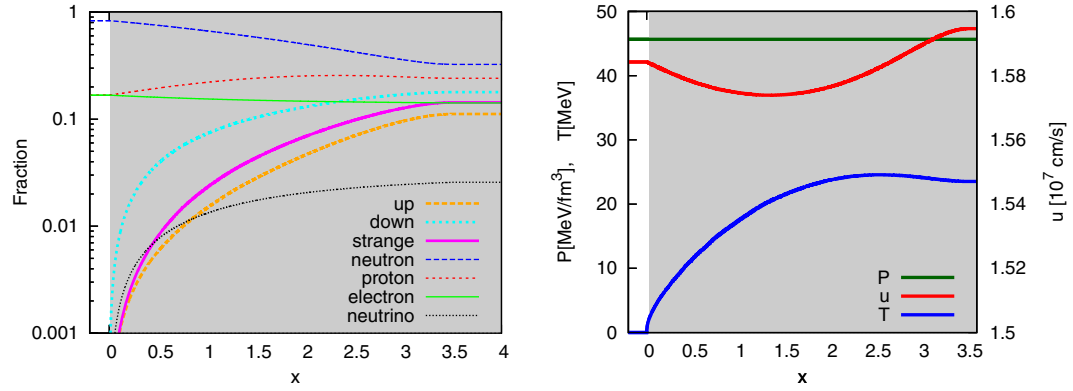

FIG. 20. The same as Fig. 13 but for NS matter with $\rho_i = 5.6 \times 10^{14}$ g/cm^3, $B^{1/4} = 130$ MeV and $\alpha_s = 0.80$.

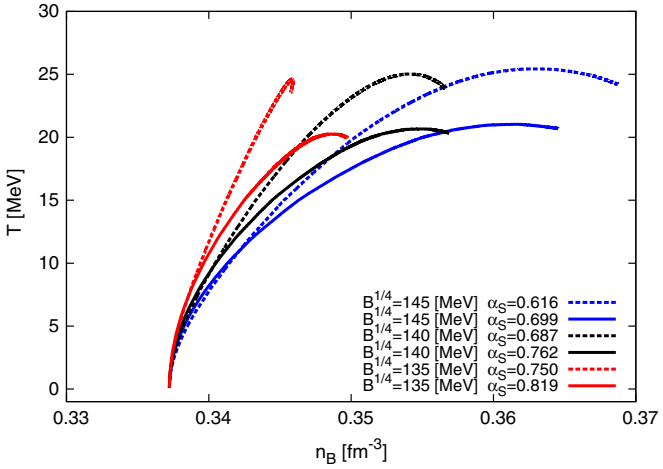

FIG. 21. The same as Fig. 15 but for the models in NS matter with $\rho_i = 5.6 \times 10^{14}$ g/cm^3 which have the same strangeness fractions at $x = 0_+$: $f_{s_Q} = 0.10$ (dashed lines) or 0.20 (solid lines).

quark phase but is later decreased due to greater repulsive forces at high densities. Figure 21 shows the results for $f_{s_Q}|_{x=0_+} = 0.1$ or 0.2. We can confirm that the results are not very different from those of the corresponding PNS cases (Fig. 15), even though all models have final states in the mixed phase, whereas the PNS cases obtain pure 3QM in their final states. The models with larger B result in higher compressions, while those with larger α suppress the rise of the temperature. The front velocities, $u_i \sim 1.4 \times 10^7$ cm/s for $f_{s_Q} = 0.1$ and $\sim 6.9 \times 10^7$ cm/s for $f_{s_Q} = 0.2$, are little affected by B and α. We hence think that $f_{s_Q}|_{x=0_+}$ is the most important parameter to determine the front velocity, since the gradient $df_s/dx|_{x=0_+}$ is sensitive to it.

V. STABILITY OF THE COMBUSTION FRONT REVISITED

Finally, we point out in this section that the stability of the deflagration front is changed in the endothermic regime. It is well known for terrestrial combustions that the deflagration front is normally unstable to deformations [28]. It is called the Darrieus-Landau instability. The combustion of nuclear fuels in white dwarfs is also subject to the instability in the type Ia supernovae. In some simulations of the conversion of neutron stars to quark stars [17,18], the instability is assumed to occur. Once developed, the instability is expected to induce a turbulence, which will then lead to the acceleration of the deflagration front. This may not be true, however, if the combustion occurs in the endothermic regime.

In order to show this, we review the linear analysis of Darrieus-Landau instability and see what is changed in the endothermic regime. In the following, we ignore the thickness of the front and treat it as a discontinuity as a common practice. We suppose that a flame front is propagating in the y directions and the unperturbed front is a plane perpendicular to the y axis. The perturbed front is assumed to be expressed as $y = f(x, t)$. The fuel ahead of and ash behind the front are approximated to be incompressible, since the front speed is much lower than the sound velocity. Then the linearized hydrodynamic equations are written both for fuel and ash as

$$\nabla \cdot \mathbf{v}_1 = 0, \tag{20}$$

$$\rho \frac{\partial \mathbf{v}_1}{\partial t} + \rho_f (\mathbf{v}_f \cdot \nabla)\mathbf{v}_1 = -\rho \nabla P_1, \tag{21}$$

where the subscript 1 implies the perturbed quantities and ρ_f and $\mathbf{v}_f$ represent the density and velocity of the fuel, respectively, in the unperturbed flow. Note that $\rho\mathbf{v} = $ const., whereas the density is assumed to be constant in the fuel and ash individually. It is also mentioned that the perturbed pressure satisfies $\Delta P_1 = 0$.

Following the common procedure in the literature [28], we assume the flame speed relation, $\mathbf{v} \cdot \mathbf{n} - v_f = $ const, and obtain the jump conditions across the flame front, which we hereafter assume to be at rest at $y = 0$ in the unperturbed flow, as follows,

$$v_{1y}|_-^+ = 0, \tag{22}$$

$$v_{1x}|_-^+ + v_f \frac{1-\alpha}{\alpha} \frac{\partial f}{\partial x} = 0, \tag{23}$$

$$P_1|_-^+ = 0, \tag{24}$$

where α ($= \rho_a/\rho_f$ with ρ_a being the density in the ash) is the ratio of the density in the ash to that in the fuel and $|_-^+$ stands for the jump across the flame front from the fuel (denoted by the suffix $-$) to the ash (denoted by the suffix $+$). The front velocity is given as

$$\frac{\partial f}{\partial t} = v_{1y-} = v_{1y+}. \tag{25}$$

Assuming the solutions in the form $v_{1x} = v_{1x}(y)e^{(ikx+\omega t)}$, $v_{1y} = v_{1y}(y)e^{(ikx+\omega t)}$, $P_1 = P_1(y)e^{(ikx+\omega t)}$ and $f = f_0 e^{(ikx+\omega t)}$ and inserting them in Eqs. (20)–(25), we obtain the dispersion relation as follows:

$$\omega = \frac{1}{1+\alpha}\left(-1 \pm \sqrt{\frac{1}{\alpha} + 1 - \alpha}\right) v_f k. \tag{26}$$

It is found that if $\alpha < 1$, which is true in the exothermic regime, the flame front is unstable, since one of the two ω's is always positive. On the other hand, when $\alpha > 1$, which corresponds to the endothermic regime, the flame front is stable because the real part is negative for both ω's.

In actual combustions in compact stars, the gravitational force and surface tension may not be neglected. Then the dispersion relation may be modified [5,28,29] as follows,

$$\omega = \frac{1}{1+\alpha}\left(-1 \pm \sqrt{\frac{1}{\alpha}+1-\alpha+g\frac{(1-\alpha^2)}{v_f^2 k}-\sigma\frac{(1+\alpha)k}{\rho_f v_f^2}}\right) \times v_f k, \tag{27}$$

where g is the gravitational acceleration and σ is the surface tension. The Darrieus-Landau instability [Eq. (26)] corresponds to the case with $g = 0$ and $\sigma = 0$. It is clear that in the exothermic regime ($\alpha < 1$), the gravitational effect tends to make the flame front unstable by buoyancy, whereas the surface tension makes it more stable. In the endothermic regime ($\alpha > 1$), on the other hand, both of them stabilize the flame front. It hence seems that the stability of the flame front in the endothermic regime is unchanged by these effects. Note that Eq. (27) is reduced in the vanishing flame-velocity and surface-tension limit to the ordinary dispersion relation for the Rayleigh-Taylor (RT) instability. It is interesting to point out that the conversion front is susceptible to the RT instability only in the exothermic regime. This seems to be in accord with some numerical results [17,18]. Since the conversion was terminated artificially when the endothermic regime was encountered in these simulations, the stability of the conversion front in the endothermic regime has not been studied numerically yet. The linear stability analysis suggests a drastic change, though. It is known for terrestrial combustions that the stability of the flame front is also affected by diffusions of heat and fuel. Although this may have some ramifications to the above discussion, we will not pursue this issue further in this paper.

VI. CONCLUSION AND DISCUSSIONS

We have studied the diffusion-induced conversion of hadronic matter to three-flavor quark matter based on the hydrodynamical description. We consider only the vicinity of the conversion region, the width of which is determined by the time scale of weak interactions times the diffusion velocity, and the plane-symmetric steady structures are investigated locally. We have studied two possible conversion scenarios: (1) HM is juxtaposed with uniform 3QM with the critical fraction of strangeness and is deconfined immediately on the time scale of strong interactions and mixed into 3QM once it trespasses the interface; the β-equilibration then occurs on the time scale of weak interactions; strange quarks are diffused in 3QM toward the interface and maintain the critical fraction of strangeness at the interface. (2) The mixed phase of HM and 3QM is initially produced, in which the volume fraction of QM is gradually increased as matter flows away from HM; uniform 3QM is reached at some point, and the evolution thereafter is identical to that in the first scenario. Note that the β-equilibration is an irreversible process accompanied by entropy generation. This series of events together with the matter motion are described, albeit phenomenologically, consistently by the hydrodynamical conservation equations and the diffusion equation for strange quarks. We have first used the simple toy model to elucidate the essential features and then employed the realistic model, in which microphysics such as EOS is more elaborated.

In the analysis with the toy model, we have demonstrated, varying model parameters rather arbitrarily in a wide range, that weak deflagration is almost always obtained both in the exothermic and endothermic regimes, the latter of which has no counterpart in terrestrial combustion but seems rather common in the conversion of HM to QM. Weak detonation is realized only when the diffusion constant is quite large, in which case the critical fraction of strangeness is small. In our realistic model, we have adopted the EOS based on relativistic mean field theory for PNS matter as well as for NS matter and employed the MIT bag model with the first-order perturbation corrections for the EOS of QM. We have observed for some EOS parameters that the mixed phase indeed lowers the free energy if the surface energy is neglected. We have also confirmed that weak deflagration is always obtained both in the exothermic and endothermic regimes. The typical values of the front velocity are $\sim 10^4$ cm/s for PNS matter with the initial temperature $T = 10$ MeV and $\sim 10^7$ cm/s for NS matter with $T = 0.01$ MeV. They are proportional to the square root of the diffusion constant and depend on the initial density as well as on the EOS parameter (e.g., the initial fraction of strangeness in the mixed phase dictated by the combination of bag constant and strong coupling constant). It is also found that the mixed phase survives up to the final state if the strong coupling constant α_s is large or the initial density is low. In such cases, the front velocity as well as the rise of temperature tend to be smaller than in the cases with uniform 3QM in the final state. We have pointed out that the laminar weak-deflagration front is stable in the endothermic regime, which is quite contrary to the ordinary exothermic combustions.

The models considered in this paper are phenomenological and certainly have much room for improvement: the EOSs adopted for HM and QM affect the critical fraction of strangeness as well as the combustion regime realized, with a softer HM and/or a harder QM being more likely to obtain an exothermic combustion as demonstrated by Herzog and Röpke [17]; the surface energy, which is neglected in this paper, will hamper the appearance of the mixed phase and should be taken into account somehow; and muons should be included in considering NS matter, although they may be minor. The results obtained in this paper are hence of qualitative nature. It should be also noted that the local approach employed in this paper cannot address any feedback from the global configuration. Since the flow

is subsonic in both up and down streams of the weak-deflagration front, the propagation of the conversion front itself changes the asymptotic states, which in turn affects the front. The global consideration is hence necessary to understand the conversion of the entire neutron star. It is stressed, however, that even in that case the local description is still valid for the structure in the conversion region.

ACKNOWLEDGMENTS

A part of the numerical calculations was carried out on a PC cluster at Center for Computational Astrophysics, National Astronomical Observatory of Japan. This work was partially supported by Grant-in-Aid for the Scientific Research from the Ministry of Education, Culture, Sports, Science and Technology, Japan (Grants No. 24103006 and No. 24244036).

[1] N. Itoh, Prog. Theor. Phys. **44**, 291 (1970).
[2] C. Alcock, E. Farhi, and A. Olinto, Astrophys. J. **310**, 261 (1986).
[3] G. Lugones and J. E. Horvath, Astron. Astrophys. **403**, 173 (2003).
[4] F. A. Williams, *Combustion Theory* (Westview Press, Boulder, CO, 1994).
[5] L. D. Landau and E. M. Lifshitz, *Fluid Mechanics* (Pergamon, London, 1987).
[6] A. F. M. Barton and A. P. W. Hodder, Chem. Rev. **73**, 127 (1973).
[7] A. V. Olinto, Phys. Lett. B **192**, 71 (1987).
[8] H. Heiselberg, G. Baym, and C. J. Pethick, Nucl. Phys. B, Proc. Suppl. **24**, 144 (1991).
[9] M. L. Olesen and J. Madsen, Nucl. Phys. B, Proc. Suppl. **24**, 170 (1991).
[10] B. Niebergal, R. Ouyed, and P. Jaikumar, Phys. Rev. C **82**, 062801 (2010).
[11] A. Bhattacharyya, S. K. Ghosh, P. S. Joarder, R. Mallick, and S. Raha, Phys. Rev. C **74**, 065804 (2006).
[12] H. T. Cho, K. Ng, and A. D. Speliotopoulos, Phys. Lett. B **326**, 111 (1994).
[13] I. Tokareva and A. Nusser, Phys. Lett. B **639**, 232 (2006).
[14] G. Lugones, O. G. Benvenuto, and H. Vucetich, Phys. Rev. D **50**, 6100 (1994).
[15] M. G. Alford, S. Han, and K. Schwenzer, Phys. Rev. C **91**, 055804 (2015).
[16] A. Drago and G. Pagliara, arXiv:1504.02795.
[17] M. Herzog and F. K. Röpke, Phys. Rev. D **84**, 083002 (2011).
[18] G. Pagliara, M. Herzog, and F. K. Röpke, Phys. Rev. D **87**, 103007 (2013).
[19] J. E. Horvath, Int. J. Mod. Phys. D **19**, 523 (2010).
[20] S. Furusawa, T. Sanada, and S. Yamada, Phys. Rev. D 043018 (2016).
[21] G. Lugones and I. Bombaci, Phys. Rev. D **72**, 065021 (2005).
[22] P. J. Steinhardt, Phys. Rev. D **25**, 2074 (1982).
[23] H. Shen, H. Toki, K. Oyamatsu, and K. Sumiyoshi, Astrophys. J. Suppl. Ser. **197**, 20 (2011).
[24] E. Farhi and R. L. Jaffe, Phys. Rev. D **30**, 2379 (1984).
[25] T. Fischer, I. Sagert, M. Hempel, G. Pagliara, J. Schaffner-Bielich, and M. Liebendörfer, Classical Quantum Gravity **27**, 114102 (2010).
[26] K. Nakamura and Particle Data Group, J. Phys. G **37**, 075021 (2010).
[27] S. Weissenborn, I. Sagert, G. Pagliara, M. Hempel, and J. Schaffner-Bielich, Astrophys. J. **740**, L14 (2011).
[28] L. D. Landau, Acta Phys.-Chim. USSR **19** (1944).
[29] J. E. Horvath and O. G. Benvenuto, Phys. Lett. B **213**, 516 (1988).